IEEE Access
Multidisciplinary | Rapid Review | Open Access Journal

Received April 2, 2019, accepted April 17, 2019, date of publication May 7, 2019, date of current version May 29, 2019.

Digital Object Identifier 10.1109/ACCESS.2019.2915263

Applying Deep Learning Approach to the Far-Field Subwavelength Imaging Based on Near-Field Resonant Metalens at Microwave Frequencies

HE MING YAO, (Student Member, IEEE), MIN LI, (Member, IEEE), AND LIJUN JIANG, (Fellow, IEEE)

Department of Electrical and Electronic Engineering, The University of Hong Kong, Hong Kong

Corresponding author: Lijun Jiang (jianglj@hku.hk)

This work was supported in part by the Research Grants Council of Hong Kong under Grant GRF 17209918, Grant GRF 17207114, and Grant GRF 17210815, in part by the Asian Office of Aerospace Research and Development under Grant FA2386-17-1-0010, in part by the National Natural Science Foundation under Grant 61271158, in part by the HKU Seed Fund under Grant 104005008, and in part by Hong Kong University Grants Committee AoE/P-04/08.

ABSTRACT In this paper, we utilize the deep learning approach for the subwavelength imaging in far-field, which is realized by the near-field resonant metalens at microwave frequencies. The resonating metalens consisting of split-ring resonators (SRRs) are equipped with the strong magnetic coupling ability and can convert evanescent waves into propagating waves using the localized resonant modes. The propagating waves in the far-field are utilized as the input of a trained deep convolutional neural network (CNN) to realize the imaging. The training data for establishing the deep CNN are obtained by the EM simulation tool. Besides, the white Gaussian noise is added into the training data to simulate the interference in the real application scenario. The proposed CNN composes of three pairs of convolutional and activation layers with one additional fully connected layer to realize the recognition, i.e., the imaging process. The feasibility of utilizing the trained deep CNN for imaging is validated by numerical benchmarks. Distinguished from the subwavelength imaging methods, the spatial response and Green's function need not be measured and evaluated in the proposed method.

INDEX TERMS Convolutional neural network, resonant metalens, machine learning, subwavelength imaging.

I. INTRODUCTION

The evanescent wave carries the high spatial frequency components containing the subwavelength information. But it exponentially decays with the distance. A large amount of research about the evanescent waves have been proposed [1]–[3]. Among them, the imaging of subwavelength information is of great importance. However, the conventional imaging systems may have difficulties in the evanescent-wave resolution due to the diffraction limit [4]–[6]. To confront this problem, various near-field approaches have been presented to enhance the evanescent wave to realize the subwavelength imaging, such as stimulated emission depletion microscopy [7], [8], stochastic optical reconstruction microscopy [9], [10], microspheres technique [11], [12], super-oscillatory lens optical microscopy [13], [14], perfect lenses [15], optical hyper lenses [16], etc. In these near-field imaging approaches, the evanescent wave is strengthened in the near field [17], [18]. However, the evanescent wave still decreases rapidly in space, which limits this kind of subwavelength imaging only in the near field. To realize the subwavelength imaging in the far field, an effective approach is presented in [19], which is realized by using a split-ring resonator (SRR) structure to convert the evanescent wave into the propagating wave. More research on SRR structure has been presented in [20], where the resonant metalens are equipped with tiny switches. Although the far-field imaging was realized in [20] by switching on and off the switch, the process could be time-consuming and has to be separately exerted on each switching-on SRR. Besides, complicated control system on

The associate editor coordinating the review of this manuscript and approving it for publication was Muhammad Sharif.

its switch might be required, which would further limit the application of the SRR structure in [20] in real scenario. Some other resonant structures, such as surface plasmons and metallic cylinders arrays, are also proposed in [21], [22]. However, the Green's function is required to connect the target and receiver to realize the target reconstruction in the far field, i.e., the far-field subwavelength image, in the microwave frequency regime. The obtaining of Green's function tremendously increases the complexity of the imaging process: (1) the Green's function is sensitive to the environment so varies largely with the environmental changes; (2) the Green's function is specific to each case [23], [24]. We may not have its convenient closed form under may practical situations.

The machine learning (ML) techniques have been introduced to advance conventional EM researches [25]–[29]. Among them, the convolutional neural networks (CNNs) [30], [31] as one of the most significant approaches in the deep learning technology are widely applied in imaging process [32], [33]. Similar to the conventional artificial neural networks (ANNs), CNNs are structured by interrelated layers. Each layer consists of basic neurons that can realize the self-optimization by learning. Like conventional neural networks, CNN also aims at training parameters in different layers and minimizing the loss function of the last layer. However, different from the conventional ANNs, CNN depends on the convolutional approach to realize the nonlinear operation and the parameter sharing to greatly reduce its parameter count. Hence, CNNs have the potential to greatly compress the big data training process and handle extreme complicated nonlinear problems. This paper presents a far-field subwavelength imaging approach that combines the near-field resonant metalens with the deep CNN to realize the imaging in the microwave frequency regime. The resonating metalens consist of the SRR structure to convert the evanescent wave into propagating wave. The propagating wave in the far field is then utilized as the input of a trained deep CNN to realize the imaging process. The advantages of the proposed method are concluded as follows: (1) Anti-interference: the method is of strong anti-interference and its accuracy is extremely high, even though large interference is added; (2) Simplicity: the Green's function is not required and a narrow frequency band is enough; (3) Effectiveness: it requires only one-time far-field simulation/measurement; (4) Flexibility: the method has the potential of being used for detection and electromagnetic monitoring.

II. IMAGING METHODOLOGY

A. RESONANT METALENS

The objective resonant metalens consists of 3×5 SRR units, as sketched in Fig. 1(a). The 3.7 GHz SRR (0.1λ) is designed on a Rogers RO 4350, with a relative permittivity 3.66, a loss tangent 0.004 and a thickness 0.8 mm, as shown in Fig. 1(b). The resonant frequency of the SRR is controlled by its effective electrical length [19]. A subwavelength loop source is located at the center of SRR on back of the substrate, as shown

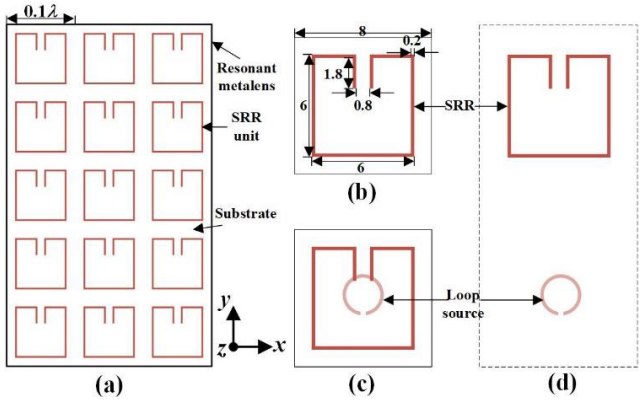

FIGURE 1. The top view of (a) resonant metalens, (b) SRR unit, (c) loop source with SRR, and (d) loop source away from SRR. (□ metal in front and □ metal in bottom).

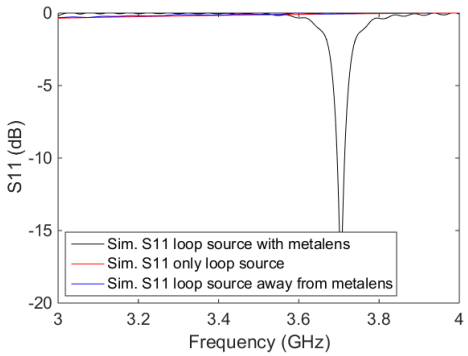

FIGURE 2. The simulated reflection coefficients of only a loop source and a loop source with SRR.

in Fig. 1(c). The SRR that is sensitive to the normal magnetic field helps to realize a strong magnetic coupling between the SRR and loop source [19]. In other words, when a loop source is located within the coupling scope of the SRR unit, it produces a localized resonance mode at around 3.7 GHz to realize the evanescent-propagating conversion for transmitting the subwavelength information to the far field. In this paper, the far-field realized gains (G) are used for imaging process. In contrast, if no loop source is put under the resonant metalens, no radiation will be received in the far field. The reflection coefficients of only a loop source (in Fig. 1(b)), a loop source with an SRR (in Fig. 1(c)) and a loop source away from SRR (in Fig. 1(d)) are simulated in Fig. 2. It can be seen that the loop source case and loop source away from SRR case both preform near-0-dB reflection coefficients, which fails to generate effective propagating waves in the far-field. In contrast, the loop source with metalens produces a localized mode resonance at around 3.7 GHz, which is helpful for the subwavelength imaging. In this case, the resolution of the proposed imaging method depends on the size of SRR unit.

B. PROPOSED CNN ARCHITECTURE

In our approach, CNNs model is utilized to convert original propagating wave data into subwavelength imaging. Because

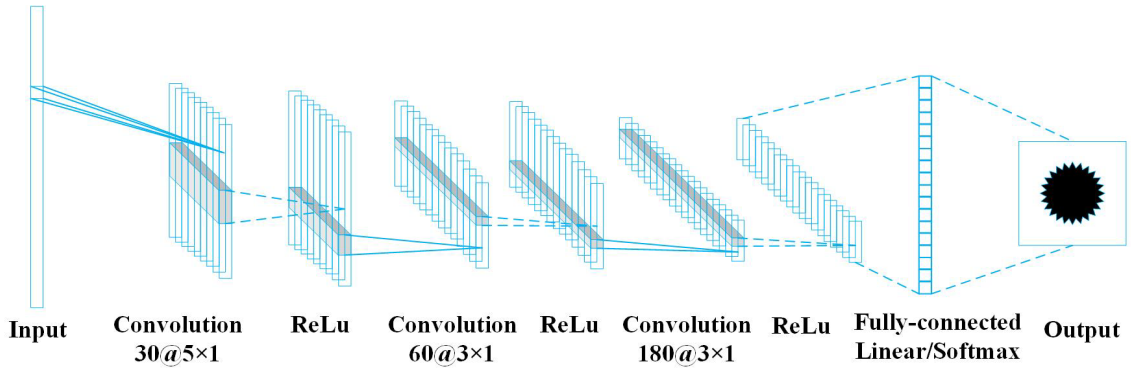

FIGURE 3. CNN architecture for subwavelength imaging.

the requirement of the huge number of training samples is difficult to fulfill by real experiments, we use simulated data to train CNNs. As the typical deep neural networks, CNNs can make use of data in the form of spatially focused images. CNNs can even utilize complex microwave field data with rich information to extract features and realize recognition and imaging [34]–[40]. In fact, though facing huge noise and complex measured microwave field data, CNNs can still succeed in realizing the far-field imaging [34]–[40]. Hence, in the process of training, we convert simulated original propagating wave gain data as inputs to our deep CNNs, and use simulated subwavelength imaging as the output. Because of the strong capability of CNN, our approach can convert the propagating wave with much stronger interference into subwavelength imaging. The regularization technique is adopted to reduce the overfitting and reduce the complex of model. Then, our CNNs model can be used to recognize our simulated subwavelength imaging.

Typical ConvNets [30], [31] consist of four types of layers: input layers, convolutional layers, pooling layers and fully-connected layers. By stacking these layers together, typical ConvNet architecture is formed. In this paper, we utilize these layers to form our convolutional neural network model for subwavelength imaging.

The internal architecture of the proposed ConvNet is shown in Fig. 3. The inputs are an $M \times 3$ matrix with field information, denoted as 'field data', where the three column values are the far-field realized gains (G) in the x-y, x-z and y-z plane, as shown in Fig. 4. For a better description, we define the x-y plane as the horizontal plane (H-plane), the x-z plane as the vertical plane 1 (V1-plane), and the y-z plane as the vertical plane 2 (V2-plane). In each plane, there are M receivers evenly located in the radiation angles (θ or ϕ) within [0°, 180°].

The convolutional layer and activation layer unit operate to capture features of input. We choose f filters (kernel) with the size of $K \times 1$ in convolutional layer. In fact, 1D kernel has wide application in stock prediction and text natural language processing [41], [42]. Convolutional layer number, kernel number f, its size K, and the stride for kernel are shown in TABLE I. Then, this convolutional layer and activation layer unit feeds into a final fully-connected layer, which predicts the subwavelength imaging in far field. This final output is used to compute the mean-squared error between the true label and the predicted label, referred to as the loss.

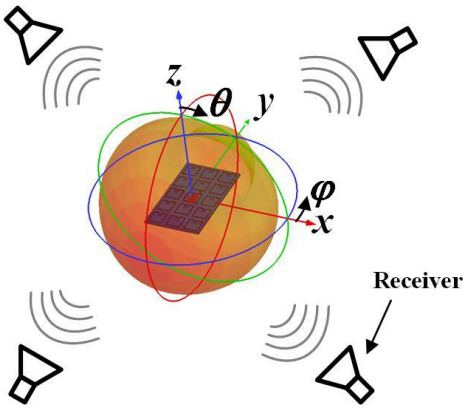

FIGURE 4. Schematic view of the subwavelength information received in the far field.

TABLE 1. CNN architecture.

Type	Filter Number	Filter Size	Stride	Input Size	Output Size
Convolution	30	5×1	[2, 1]	180×3×1	90×3×30
ReLu				90×3×30	90×3×30
Convolution	60	3×1	[3, 1]	90×3×30	30×3×60
ReLu				30×3×60	30×3×60
Convolution	180	3×1	[3, 1]	30×3×60	10×3×180
ReLu				10×3×180	10×3×180
Fully-connected				10×3×180	5400×1
Softmax				5400×1	7
Loss function					

Our method is benchmarked in Matlab 2018b with Deep Learning Toolbox [43]. The mean-squared error loss function is optimized by stochastic gradient descent. The learning rate, chosen as 0.01, is the hyper-parameter in our model. We can control training error by declining the learning rate. The training is done by full batch. L2 regularization is applied to prevent over-fitting and improve prediction accuracy [44].

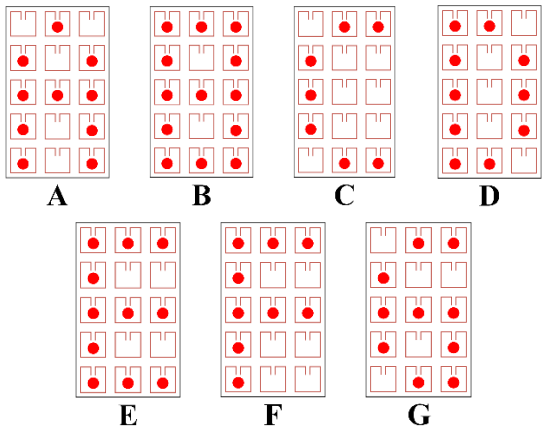

FIGURE 5. Schematic view of the alphabet-shaped subwavelength source target.

C. APPLYING CNN TO FAR-FIELD IMAGING

By putting the resonant metalens on the loop sources, the propagating wave converted from the evanescent wave can be noted by the far-field receivers. Then, the received propagating wave containing subwavelength information even with interference can be dealt with the proposed CNNs, i.e., realizing the far-field subwavelength imaging.

The design procedures of the proposed method for far-field subwavelength imaging are formulated into the following three steps:

Step 1: Obtaining far-field results: The resonant metalens are installed above the target source to be imaged, so that radiation gain G from the metalens-added target can be noted by receivers in the far field;

Step 2: CNN model training: The received radiation signals polluted by noise is used as the training data (training input) for the proposed CNN model, while the corresponding target source are used as training output. The added noise is to imitate the complex environment in reality, such as fabrication tolerance, the measurement tolerance, etc. [45], [46]. Moreover, compared with training data without noise, it is very easy to add noise into the training data to dramatically improve the noise tolerance and imaging performance of the whole method.

Step 3: Far-field imaging: Using the trained CNN model, the image of the target source can be recognized from the newly received radiation signals even with large interference.

III. NUMERICAL RESULTS

A. IMAGING FOR ALPHABET-SHAPED SOURCE USING THREE-PLANE RADIATION GAIN

In this section, the alphabet-shaped target sources from 'A' to 'G' are used, as demonstrated in Fig. 5. Following the design methodology in Section II, the detailed processes are presented as follows:

Step 1: Obtaining far-field results: The resonant metalens are installed above the alphabet-shaped sources and the far-field realized gains (G) at the H, V1 and V2 planes are obtained using CST Microwave Studio [47]. In reality, the

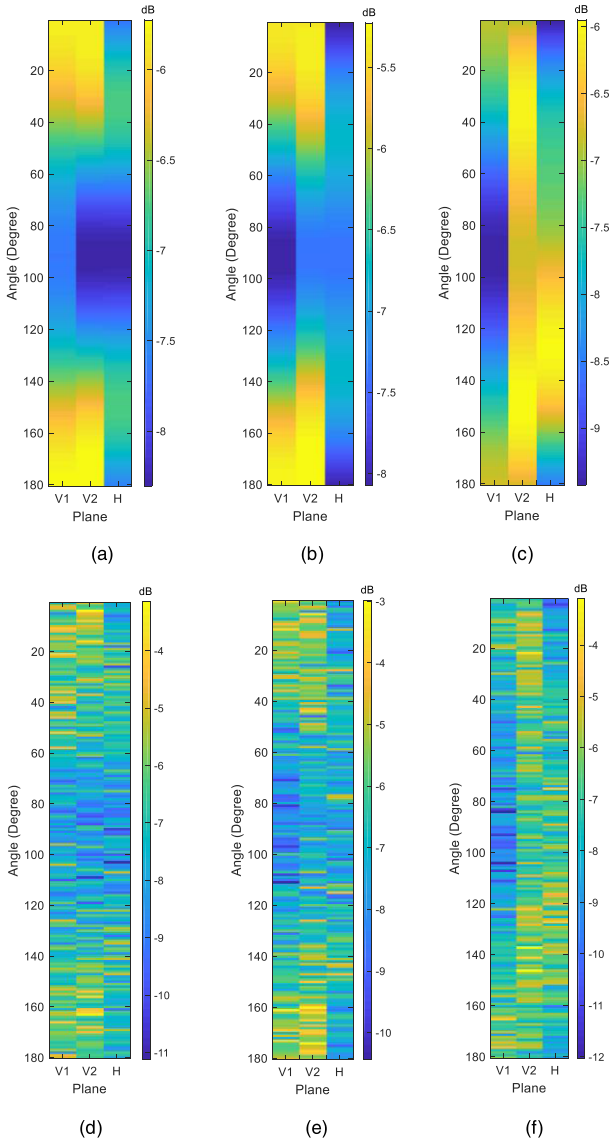

FIGURE 6. Accurate 'field data' for subwavelength alphabet-shaped source: (a) A; (b) B; (c) C. 'field data' with noise for subwavelength alphabet-shaped source: (d) A; (e) B; (f) C.

far-field gains (G) can be obtained by receivers with the aid of the vector network analyzer (VNA).

Step 2: CNN model training: For training, the size of each input data is $M \times 3$ with $M = 180$. Considering the interference in real application scenario, the random noise with signal-to-noise ratio (SRN) up to 0dB is added to the received field information (Fig. 6(a)-(c)) to form the input training data (Fig. 6(d)-(f)), as shown in Fig. 6. Here, the data for alphabet sources 'D-G' are not demonstrated to save space. Compared Figs. (d-f) with (a-c), it can be seen that the final 'field data' is very different from the original ones. With this extremely small SNR, it is difficult for conventional methods to realize the subwavelength imaging [48]. To train the proposed deep CNN, we utilized 7000 'field data' with random noise as the inputs and the corresponding alphabet-shaped sources are used as the outputs.

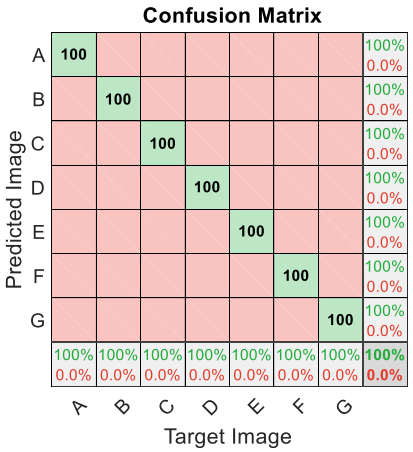

FIGURE 7. Performance of our proposed method for subwavelength imaging. The green percentage is the success rate, while the red percentage is the failure rate.

Step 3: Far-field imaging: Another 700 groups of 'field data' with random noise (SNR = 0dB) as inputs and their corresponding sources as outputs are used to test the feasibility of the proposed CNN model. As a result, the image of the target sources can be realized despite of such large interference.

The performances of the proposed trained deep CNN are presented in Fig. 7. It can be seen that the proposed CNNs can realize the subwavelength imaging, i.e., recognizing the alphabet-shaped source image under large interference, with zero error.

Moreover, the further trails present that the proposed deep CNNs trained on the data set with the noise in the level of SNR = 0 dB or any SNR>0 dB can all succeed in realizing far field imaging and provide the same accurate result with zero error as that shown in Fig.7.

B. IMAGING FOR ALPHABET-SHAPED SOURCE USING ONE-PLANE RADIATION GAIN

To make the proposed method more applicable, two improvements on the 'field data' are made: (1) Only the far-field realized gains (G) in the H plane instead of three planes are used as inputs. (2) In ***Step 3***, the newly received far-field realized gains (G) for imaging are obtained from the radiation angles ($\phi = 0°, 6°, \ldots, 180°$). As a result, the far-field realized gains (G) are converted to the CNN model as a $M/6$ vector, which is much smaller than $M \times 3$ in Section III A.

The specific process is as follows:

Step 1: Obtaining far-field results: The resonant metalens are installed above the alphabet-shaped sources and the far-field realized gain (G) only in the H plane is obtained using CST Microwave Studio.

Step 2: CNN model training: For training, the size of input data is $M \times 1$ ($M = 180$). The CNN parameters (Filter Number, Filter Size, and Stride Size) in TABLE 1 is used again, since the application scenario is not changed. The random noise (SRN = 10 dB) is added to the received field information (Fig. 8(a)-(c)) to form the input training data. To train the proposed deep CNN, we utilized 7000 'field data' with random noise as the inputs and the corresponding alphabet-shaped sources are used as the outputs.

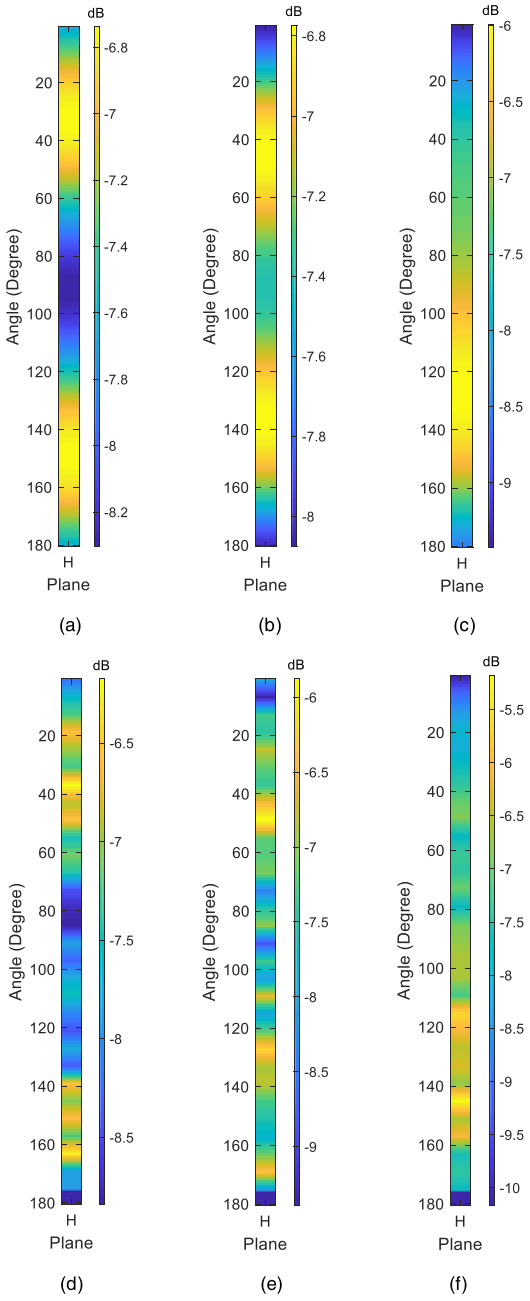

FIGURE 8. Accurate 'field data' in the H plane for subwavelength alphabet-shaped source: (a) A; (b) B; (c) C. Interpolated 'field data' in the H plane with noise for subwavelength alphabet-shaped source: (d) A; (e) B; (f) C.

Step 3: Far-field imaging: Another 700 groups of 'field data' with random noise (SNR = 10 dB) as inputs and their corresponding sources as outputs are used to test the feasibility of the proposed CNN model. As stated above, the far-field gain (G) data decrease to a $M/6$ vector. Hence, the linear interpolation method is used to compensate the received field information so that the size of each input is still $M \times 1$, as shown in Fig. 8(d)-(f). As a result, the image

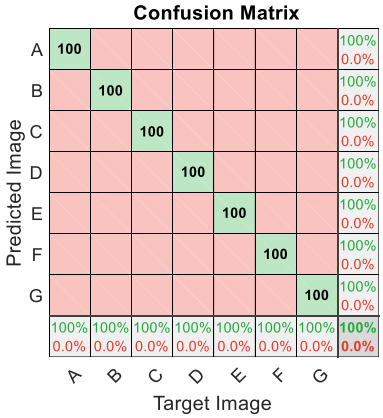

FIGURE 9. Performance of the proposed method for subwavelength imaging by only using far-field realized gains (G) in the H plane. The green percentage is the success rate, while the red percentage is the failure rate.

of the target sources can be obtained despite of the large interference and less field data.

The performances of the proposed trained deep CNN are presented in Fig. 9. It can be seen that the proposed CNNs can realize the subwavelength imaging, i.e., recognizing the alphabet-shaped source image under large interference, with zero error.

C. IMAGING FOR ALPHABET-SHAPED SOURCE USING ONE-PLANE RADIATION GAIN IN COMPLEX ENVIRONMENT

In this section, the proposed method is utilized in more challenging environment, presented in Fig. 10, where the alphabet-shaped target sources are surrounded by concrete walls. The detailed parameters of the used concrete walls are as follows: the thermal conductivity is 1.7 $W/K \cdot m$, the material density is 2400 kg/m^3, and the heat capacity is 0.8 $kJ/K{\cdot}kg$. The format of 'field data' and the detailed imaging processes and in the Section III B are still used in this section. The Fig. 10(b) shows the accurate 'field data' in the H plane for subwavelength alphabet-shaped source 'A', while the Fig. 10(c) presents the interpolated 'field data' in the H plane with noise for subwavelength alphabet-shaped source 'A'. Here, the data for alphabet sources 'B-G' are not demonstrated to save space.

The performances of the trained deep CNN are shown in Fig. 11. It is evident that the proposed CNNs can realize the subwavelength imaging, i.e., recognizing the alphabet-shaped source image even when the sources are completely enclosed.

D. DISCUSSION

The numerical examples above present that the trainable deep CNN can successfully recognize the subwavelength source under large interference. The unavoidable interference in reality can be overcome thanks to its strong feature-extracted ability for recognition [49]–[51]. Besides, the usage of deep CNN also avoids the environmental sensitivity and the need for obtaining Green's function by conventional methods.

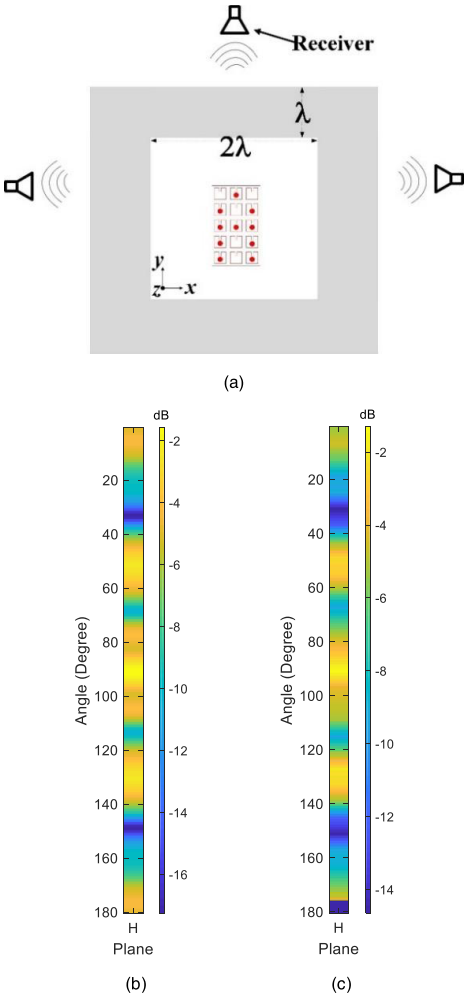

FIGURE 10. (a) Top view of the alphabet-shaped subwavelength source target with the resonant metalens surrounded concrete walls. (b) Accurate 'field data' in the H plane for subwavelength alphabet-shaped source 'A'. (c) Interpolated 'field data' in the H plane with noise for subwavelength alphabet-shaped source 'A'.

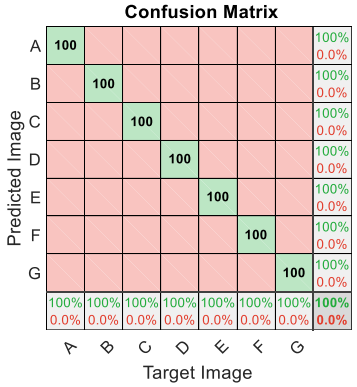

FIGURE 11. Performance of the proposed method for subwavelength imaging by only using far-field realized gains (G) in the H plane in complex environment. The green percentage is the success rate, while the red percentage is the failure rate.

Thus, the proposed method has the potential to be used in extremely harsh environment, such as the space with large background radiation.

Three examples above demonstrate that the proposed far-field imaging method with near-field resonant metalens can effectively realize imaging for the subwavelength targets under big interference without using the Green's function.

IV. CONCLUSION

In this paper, the near-field resonant metalens are combined with the deep CNN to realize subwavelength imaging in the far-field at microwave frequencies. The 3×5 split-ring resonator (SRR) units are utilized to form the resonant metalens with strong magnetic coupling ability. The resonant metalens convert evanescent wave in the near field into propagating wave. The received far-field data is utilized as inputs of a trained deep CNN to realize subwavelength imaging. The possible strong interference in real application scenario is considered in the training data. Numerical examples have demonstrated the feasibility of utilizing our CNN to realize subwavelength imaging. The spatial response and Green's function are not needed in the proposed method. This method can be used for subwavelength imaging, detection, and electromagnetic monitoring in complex environments.

REFERENCES

[1] J. B. Pendry, "Negative refraction makes a perfect lens," *Phys. Rev. Lett.*, vol. 85, no. 18, pp. 3966–3969, Oct. 2000.
[2] X. S. Rao and C. K. Ong, "Amplification of evanescent waves in a lossy left-handed material slab," *Phys. Rev. B, Condens. Matter*, vol. 68, no. 11, Sep. 2003, Art. no. 113103.
[3] F. de Fornel, *Evanescent Waves: From Newtonian Optics to Atomic Optics*, 2nd ed. Berlin, Germany: Springer, 2010.
[4] E. Abbe, "Beiträge zur theorie des mikroskops und der mikroskopischen wahrnehmung," *Archiv für Mikroskopische Anatomie*, vol. 9, no. 1, pp. 413–418, Dec. 1873.
[5] Z. Jacob, L. V. Alekseyev, and E. Narimanov, "Optical hyperlens: Far-field imaging beyond the diffraction limit," *Opt. Express*, vol. 14, no. 18, pp. 8247–8256, Sep. 2006.
[6] S. So, M. Kim, D. Lee, D. M. Nguyen, and J. Rho, "Overcoming diffraction limit: From microscopy to nanoscopy," *Appl. Spectrosc. Rev.*, vol. 53, nos. 2–4, pp. 290–312, Apr. 2018.
[7] J. Fischer and M. Wegener, "Three-dimensional direct laser writing inspired by stimulated-emission-depletion microscopy," *Opt. Mater. Express*, vol. 1, no. 4, pp. 614–624, Aug. 2011.
[8] T. A. Klar, M. Dyba, and S. W. Hell, "Stimulated emission depletion microscopy with an offset depleting beam," *Appl. Phys. Lett.*, vol. 78, no. 4, pp. 393–395, 2001.
[9] M. J. Rust, M. Bates, and X. Zhuang, "Sub-diffraction-limit imaging by stochastic optical reconstruction microscopy (STORM)," *Nature Methods*, vol. 3, no. 10, pp. 793–796, 2006.
[10] E. Betzig *et al.*, "Imaging intracellular fluorescent proteins at nanometer resolution," *Science*, vol. 313, no. 5793, pp. 1642–1645, 2006.
[11] A. Darafsheh, N. I. Limberopoulos, J. S. Derov, D. E. Walker, and V. N. Astratov, "Advantages of microsphere-assisted super-resolution imaging technique over solid immersion lens and confocal microscopies," *Appl. Phys. Lett.*, vol. 104, no. 6, Jan. 2014, Art. no. 061117.
[12] K. W. Allen *et al.*, "Overcoming the diffraction limit of imaging nanoplasmonic arrays by microspheres and microfibers," *Opt. Express*, vol. 23, pp. 24484–24496, Sep. 2015.
[13] E. T. F. Rogers *et al.*, "A super-oscillatory lens optical microscope for subwavelength imaging," *Nature Mater.*, vol. 11, pp. 432–435, Mar. 2012.
[14] T. Liu, J. Tan, J. Liu, and H. Wang, "Vectorial design of super-oscillatory lens," *Opt. Express*, vol. 21, no. 13, pp. 15090–15101, 2013.
[15] W. H. Wee and J. B. Pendry, "Universal evolution of perfect lenses," *Phys. Rev. Lett.*, vol. 106, Apr. 2011, Art. no. 165503.
[16] S. Xu *et al.*, "Realization of deep subwavelength resolution with singular media," *Sci. Rep.*, vol. 4, Jun. 2014, Art. no. 5212.
[17] L. Markley and G. V. Eleftheriades, "A near-field probe for subwavelength-focused imaging," in *IEEE MTT-S Int. Microw. Symp. Dig.*, Jun. 2009, pp. 281–284.
[18] A. Ludwig, C. D. Sarris, and G. V. Eleftheriades, "Near-field antenna arrays for steerable sub-wavelength magnetic-field beams," *IEEE Trans. Antennas Propag.*, vol. 62, no. 7, pp. 3543–3556, Jul. 2014.
[19] G. Boudarham *et al.*, "Spectral imaging of individual split-ring resonators," *Phys. Rev. Lett.*, vol. 105, Dec. 2010, Art. no. 255501.
[20] R. Wang, B.-Z. Wang, Z.-S. Gong, and X. Ding, "Far-field subwavelength imaging with near-field resonant metalens scanning at microwave frequencies," *Sci. Rep.*, vol. 5, Jun. 2015, Art. no. 11131.
[21] F. Wei *et al.*, "Wide field super-resolution surface imaging through plasmonic structured illumination microscopy," *Nano Lett.*, vol. 14, pp. 4634–4639, Jul. 2014.
[22] F. Lemoult, G. Lerosey, J. de Rosny, and M. Fink, "Resonant metalenses for breaking the diffraction barrier," *Phys. Rev. Lett.*, vol. 104, May 2010, Art. no. 203901.
[23] M. Memarian and G. V. Eleftheriades, "Evanescent-to-propagating wave conversion in sub-wavelength metal-strip gratings," *IEEE Trans. Microw. Theory Techn.*, vol. 60, no. 12, pp. 3893–3907, Dec. 2012.
[24] S. Steshenko, F. Capolino, P. Alitalo, and S. Tretyakov, "Effective model and investigation of the near-field enhancement and subwavelength imaging properties of multilayer arrays of plasmonic nanospheres," *Phys. Rev. E, Stat. Phys. Plasmas Fluids Relat. Interdiscip. Top.*, vol. 84, Jul. 2011, Art. no. 016607.
[25] H. M. Yao, L. Jiang, and Y. W. Qin, "Machine learning based method of moments (ML-MoM)," in *Proc. Int. Symp. IEEE Antennas Propag. USNC/URSI Nat. Radio Sci. Meeting*, San Diego, CA, USA, Jul. 2017, pp. 973–974.
[26] T. Shan, X. Dang, M. Li, F. Yang, S. Xu, and J. Wu, "Study on a 3D possion's equation slover based on deep learning technique," in *Proc. IEEE Int. Conf. Comput. Electromagn.*, Mar. 2018, pp. 1–3.
[27] H. M. Yao and L. J. Jiang, "Machine learning based neural network solving methods for the FDTD method," in *Proc. Int. Symp. IEEE Antennas Propag. USNC/URSI Nat. Radio Sci. Meeting*, Boston, MA, USA, Jul. 2018, pp. 2321–2322.
[28] H. H. Zhang and R. S. Chen, "Coherent processing and superresolution technique of multi-band radar data based on fast sparse Bayesian learning algorithm," *IEEE Trans. Antennas Propag.*, vol. 62, no. 12, pp. 6217–6227, Dec. 2014.
[29] H. M. Yao and L. Jiang, "Machine-learning-based PML for the FDTD method," *IEEE Antennas Wireless Propag. Lett.*, vol. 18, no. 1, pp. 192–196, Jan. 2019.
[30] A. Krizhevsky, I. Sutskever, and G. E. Hinton, "ImageNet classification with deep convolutional neural networks," *Commun. ACM*, vol. 60, no. 2, pp. 84–90, Jun. 2012.
[31] Y. Zhang, D. Zhao, J. Sun, G. Zou, and W. Li, "Adaptive convolutional neural network and its application in face recognition," *Neural Process. Lett.*, vol. 43, no. 2, pp. 389–399, 2016.
[32] C. Dong, C. C. Loy, K. He, and X. Tang, "Image super-resolution using deep convolutional networks," *IEEE Trans. Pattern Anal. Mach. Intell.*, vol. 38, no. 2, pp. 295–307, Feb. 2015.
[33] B. Sahiner *et al.*, "Classification of mass and normal breast tissue: A convolution neural network classifier with spatial domain and texture images," *IEEE Trans. Med. Imag.*, vol. 15, no. 5, pp. 598–610, Oct. 1996.
[34] T. Song, L. Kuang, L. Han, Y. Wang, and Q. H. Liu, "Inversion of rough surface parameters from SAR images using simulation-trained convolutional neural networks," *IEEE Geosci. Remote Sens. Lett.*, vol. 15, no. 7, pp. 1130–1134, Jul. 2018.
[35] Z. Wei and X. Chen, "Deep-learning schemes for full-wave nonlinear inverse scattering problems," *IEEE Trans. Geosci. Remote Sens.*, vol. 57, no. 4, pp. 1849–1860, Apr. 2019. doi: 10.1109/TGRS.2018.2869221.
[36] Y. Zhou, H. Wang, F. Xu, and Y.-Q. Jin, "Polarimetric SAR image classification using deep convolutional neural networks," *IEEE Geosci. Remote Sens. Lett.*, vol. 13, no. 12, pp. 1935–1939, Dec. 2016.
[37] L. Li, L. G. Wang, F. L. Teixeira, C. Liu, A. Nehorai, and T. J. Cui, "DeepNIS: Deep neural network for nonlinear electromagnetic inverse scattering," *IEEE Trans. Antennas Propag.*, vol. 67, no. 3, pp. 1819–1825, Mar. 2019.
[38] X. X. Zhu *et al.*, "Deep learning in remote sensing: A comprehensive review and list of resources," *IEEE Geosci. Remote Sens. Mag.*, vol. 5, no. 4, pp. 8–36, Dec. 2017.
[39] Z. Lin, K. Ji, M. Kang, X. Leng, and H. Zou, "Deep convolutional highway unit network for SAR target classification with limited labeled training data," *IEEE Trans. Geosci. Remote. Sens. Lett.*, vol. 14, no. 7, pp. 1091–1095, Jul. 2017.

[40] S. Chen, H. Wang, F. Xu, and Y. Q. Jin, "Target classification using the deep convolutional networks for SAR images," *IEEE Trans. Geosci. Remote Sens.*, vol. 54, no. 8, pp. 4806–4817, Aug. 2016.
[41] X. Ding, Y. Zhang, T. Liu, and J. Duan, "Deep learning for event-driven stock prediction," in *Proc. 24th Int. Conf. Artif. Intell. (IJCAI)*, 2015, pp. 2327–2333.
[42] K. Tymoshenko, D. Bonadiman, and A. Moschitti, "Convolutional neural networks vs. convolution kernels: Feature engineering for answer sentence reranking," in *Proc. HLT-NAACL*, 2016, pp. 1268–1278.
[43] P. Kim, *MATLAB Deep Learning*. New York, NY, USA: Apress, 2017.
[44] A. Y. Ng, "Feature selection, L1 vs. L2 regularization, and rotational invariance," in *Proc. 21st Int. Conf. Mach. Learn.*, 2004, pp. 78–86.
[45] J. A. Russer and P. Russer, "Modeling of noisy EM field propagation using correlation information," *IEEE Trans. Microw. Theory Techn.*, vol. 63, no. 1, pp. 76–89, Jan. 2015.
[46] K. Haneda, E. Kahra, S. Wyne, C. Icheln, and P. Vainikainen, "Measurement of loop-back interference channels for outdoor-to-indoor full-duplex radio relays," in *Proc. 4th Eur. Conf. Antennas Propag.*, Apr. 2010, pp. 1–5.
[47] *3D EM Simulation Software*, Studio, CST Microwave, Computer Simulation Technology, Framingham, MA, USA, 2014. [Online]. Available: http://www.cst.com
[48] A. Neice, "Methods and limitations of subwavelength imaging," *Adv. Imag. Electron Phys.*, vol. 163, pp. 117–140, Jan. 2010.
[49] A. Romero, C. Gatta, and G. Camps-Valls, "Unsupervised deep feature extraction for remote sensing image classification," *IEEE Trans. Geosci. Remote Sens.*, vol. 54, no. 3, pp. 1349–1362, Mar. 2016.
[50] Y. Chen, H. Jiang, C. Li, X. Jia, and P. Ghamisi, "Deep feature extraction and classification of hyperspectral images based on convolutional neural networks," *IEEE Trans. Geosci. Remote Sens.*, vol. 54, no. 10, pp. 6232–6251, Oct. 2016.
[51] V. Jain and S. Seung, "Natural image denoising with convolutional networks," in *Proc. Neural Inf. Process. Syst.*, 2008, pp. 769–776.

HE MING YAO received the B.S. degree in information and computing science and the M.S. degree in electronic and communication engineering from Beihang University, Beijing, China, in 2013 and 2016, respectively. He is currently pursuing the Ph.D. degree with the Department of Electrical and Electronic Engineering, The University of Hong Kong, Hong Kong. His research interests include CEM, EMC/EMI, machine learning, and advanced materials.

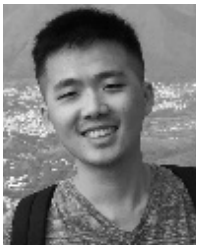

MIN LI (S'14–M'18) received the B.S. degree from UESTC, Chengdu, China, in 2014, and the Ph.D. degree from The University of Hong Kong, Hong Kong, in 2018, where he is currently a Postdoctoral Researcher with the Department of Electrical and Electronic Engineering. His current research interests include antenna design and multiple-input multiple-output antenna decoupling.

LIJUN JIANG (S'01–M'04–SM'13–F'19) received the B.S. degree in electrical engineering from the Beijing University of Aeronautics and Astronautics, Beijing, China, in 1993, the M.S. degree from Tsinghua University, Beijing, in 1996, and the Ph.D. degree from the University of Illinois at Urbana–Champaign, Champaign, IL, USA, in 2004.

From 1996 to 1999, he was an Application Engineer with the Hewlett-Packard Company. Since 2004, he has been a Postdoctoral Researcher, a Research Staff Member, and a Senior Engineer with the IBM T. J. Watson Research Center, Yorktown Heights, NY, USA. Since 2009, he has been an Associate Professor with the Department of Electrical and Electronic Engineering, The University of Hong Kong, Hong Kong. He served as a Scientific Consultant with Hong Kong Applied Science and Technology Research Institute Company Ltd., from 2010 to 2011. Since 2013, he has been a Senior Visiting Professor with Tsinghua University. He has been serving as a Panelist on the Expert Review Panel of the Hong Kong Research and Development Center for Logistics and Supply Chain Management Enabling Technologies, since 2013. He was the Semiconductor Research Cooperation (SRC) Industrial Liaison for several academic projects. He has been involved collaboratively with many international researchers.

Dr. Jiang is the IEEE AP-S Member, the IEEE MTT-S Member, the IEEE EMC-S Member, an ACES Member, and a member of the Chinese Computational Electromagnetics Society. He was a Scientific Committee Member of the 2010 IEEE Simulation and Modeling of Emerging Electronics, the Special Session Organizer of the IEEE EDAPS, the IEEE Electromagnetic Compatibility Society, the Applied Computational Electromagnetics Society, the Asia-Pacific Radio Science Conference, and the Progress in Electromagnetics Research Symposium and a Co-Organizer of the HKU Computational Science and Engineering Workshops, from 2010 to 2012. He has been an Elected TPC Member of the IEEE Electrical Design of Advanced Packaging and Systems Symposium (EDAPS), since 2010, and the IEEE Electrical Performance of Electronic Packaging, since 2014. He was a TPC Member of the 2013 IEEE International Conference on Microwave Technology & Computational Electromagnetics. He has been a TC-9 Member and a TC-10 Member of the IEEE Electromagnetic Compatibility Society, since 2011. He received the IEEE MTT Graduate Fellowship Award, in 2003, and the Y. T. Lo Outstanding Research Award, in 2004. He was the Session Chair of many international conferences. He was the TPC Chair of the 7th International Conference on Nanophotonics/the 3rd Conference on Advances in Optoelectronics and Micro/Nano Optics, the TPC Co-Chair of the 12th International Workshop on Finite Elements for Microwave Engineering, and the 2013 International Workshop on Pulsed Electromagnetic Field at Delft, The Netherlands, and the General Chair of the 2014 IEEE 14th HK AP/MTT Postgraduate Conference. He was an Associate Guest Editor of the PROCEEDINGS OF THE IEEE special issue, from 2011 to 2012. He is also an Associate Editor of the IEEE TRANSACTIONS ON ANTENNAS AND PROPAGATION and *Progress in Electromagnetics Research*. He also serves as a Reviewer for the IEEE Transactions on several topics and other primary electromagnetics and microwave related journals.